Journal of The
Electrochemical Society

The Electrochemical Society
Advancing solid state & electrochemical science & technology

OPEN ACCESS

Suppression of Transition Metal Dissolution in Mn-Rich Layered Oxide Cathodes with Graphene Nanocomposite Dry Coatings

To cite this article: David A. Boyd *et al* 2024 *J. Electrochem. Soc.* **171** 100532

View the article online for updates and enhancements.

You may also like

- Beneficial Effects of Oxide-Based Additives on Li-and Mn-rich Cathode Active Materials
Louis Hartmann, Cheuck Hin Ching, Tanja Zünd et al.
- 2024 roadmap for sustainable batteries
Magda Titirici, Patrik Johansson, Maria Crespo Ribadeneyra et al.
- Status and outlook for lithium-ion battery cathode material synthesis and the application of mechanistic modeling
Kunal Pardikar, Jake Entwistle, Ruihuan Ge et al.

PAT-Tester-x-8 Potentiostat:
Modular Solution for Electrochemical Testing!

EL-CELL®
electrochemical test equipment

✓ Flexible Setup with up to 8 Independent Test Channels!
Each with a fully equipped Potentiostat, Galvanostat and EIS!

✓ Perfect Choice for Small-Scale and Special Purpose Testing!
Suited for all 3-electrode, optical, dilatometry or force test cells from EL-CELL.

✓ Complete Solution with Extensive Software!
Plan, conduct and analyze experiments with EL-Software.

✓ Small Footprint, Easy to Setup and Operate!
Usable inside a glove box. Full multi-user, multi-device control via LAN.

Scan me!

Contact us:
☎ +49 40 79012-734
✉ sales@el-cell.com
🌐 www.el-cell.com

This content was downloaded from IP address 128.195.95.45 on 14/05/2025 at 21:47

Journal of The Electrochemical Society, 2024 **171** 100532

Suppression of Transition Metal Dissolution in Mn-Rich Layered Oxide Cathodes with Graphene Nanocomposite Dry Coatings

David A. Boyd,[1,z] Cullen M. Quine,[1] Jasmina Pasalic,[2] Channing Ahn,[1] William C. West,[2] and Brent Fultz[1]

[1] *Department of Applied Physics and Materials Science, California Institute of Technology, Pasadena, CA 91125, United States of America*
[2] *Jet Propulsion Laboratory, California Institute of Technology, Pasadena, CA 91109, United States of America*

The growing demand for lithium-ion batteries (LIBs) and the reliance on scarce metals in cathode active materials (CAMs) have prompted a search for sustainable alternatives. However, the performance of Mn-rich CAMs formulated with less Co suffer from transition metal dissolution (TMD). TMD can be suppressed by applying a thin film of carbon or oxide to the CAM but the assumed need for a continuous film necessitates bottom-up coating methods. This has been a challenge for LIB production as well as limiting material choices. Here we show that particulate coatings can also suppress TMD, allowing for scalable, material-independent, dry coating methods. Dry coating the Mn-rich CAM surfaces with graphene encapsulated nanoparticles (GEN) (1 wt %) suppresses TMD while nearly doubling the cycle life and improving rate capacities up to 42% under stressful conditions. The ability to suppress TMD is attributed to the unique chemical and electronic properties of the GEN produced by plasma enhanced chemical vapor deposition. The method is general and could provide a scalable path to CAM with less Co.

[DOI: 10.1149/1945-7111/ad867f]

Manuscript submitted August 17, 2024; revised manuscript received October 2, 2024. Published November 1, 2024.

Supplementary material for this article is available online

Lithium-ion batteries (LIBs) have widespread applications in portable electronics and electric vehicles (EVs) owing to their high specific energy (120–270 $\mathrm{Whr\,kg^{-1}}$) and high energy density (300–750 $\mathrm{Wh\,l^{-1}}$). Their continued success is placing increasing demands on further improvements in performance and cost. Shorter charging times and lower cost of ownership are essential for EV adoption,[1] and improvements in cathode technology can help address both. The rate capability of a cell, inversely related to its charging time, is fundamentally determined by the ionic and electronic transport properties of the cathode at normal operating temperatures. A working cathode comprises particulate cathode active material (CAM), binders, and conductive agents, forming a network with interfaces at the liquid electrolyte and at the solid electrode. These interfaces can affect the lithium ion diffusion, the electronic conductivity, and charge transfer. Stabilizing the interfaces at the CAM could lead to increased rate capabilities and longer cycle life.[2] Cathodes are the primary cost drivers in LIB,[3] and improvements that increase cell lifetimes could reduce the cost of EV ownership. However, advances in cathode performance have come, in part, at the expense of limited mineral resources. For example, the constituent components of state-of-the-art (SOA) layered oxides such as NMC, are Li, Mn, Ni, and Co. Cobalt, most notably, is not only scarce, it is also subject to the uncertainties of supply chains and the economics, ethics, and politics of mining and ore processing, making the need for lower cost alternatives self-evident.[4,5] A challenge for LIB cathodes is to do more with less: increase rate capability and cycle life while using less high-value materials.

Although capacity values for SOA cathodes are approaching 200 mAh/g and 500+ cycles, under moderate conditions, performance can be fleeting as the CAM can suffer performance loss for a variety of reasons including deleterious side-interactions with the electrolyte,[6] mechanical stresses during charge and discharge,[7] phase transformations,[8] Jahn-Teller distortion (JTD),[9] and transition-metal dissolution (TMD).[10–15] TMD is an unwanted effect that occurs when transition metals in the CAM are dissolved and typically reduced at the anode upon cycling, and it is generally associated with degradation of the solid electrolyte interphase (SEI).[16,17] Not only does TMD affect the cathode crystallographic phase, but the dissolution of Mn ions[18] can destabilize the electrolyte and the SEI and degrade the graphite anode[12,19,20] TMD limits the use of Mn-rich CAM such as $LiMn_2O_4$ (LMO) and $Li_{1.2}Ni_{0.13}Mn_{0.54}Co_{0.13}O_2$ (LNMC), which are desirable for their performance while employing relatively less Co or Ni compared to SOA NMC, e.g. $LiNi_{0.8}Mn_{0.1}Co_{0.1}O_2$ (NMC811).[9,21]

One approach to improving performance is to apply coatings to the CAM. Thin coatings applied directly to the CAM fundamentally serve to protect and stabilize the interface between the cathode and the electrolyte, providing resistance toward chemical attack by acidic and alkaline species and suppressing electrolyte decomposition and unconstrained growth of the cathode electrolyte interphase (CEI). Amorphous or crystalline coatings of oxides, as well as fluorides, phosphates, lithium composites, and glasses, are commonly used and can also offer such benefits as improving Li^+ diffusion, scavenging by-product HF, providing strain relaxation, suppressing TMD, and even improving low-temperature performance.[6,22–30] Although these materials provide durable, stable coatings, they possess marginal electronic and ionic conductivity, which can limit fast charging.

An alternative is carbon. Carbon is electronically and thermally conductive, has high Li diffusivity, and is inherently compatible with current battery materials. Carbon coatings have been found to offer a variety of benefits, including better capacity, rate capability, cycling stability, and capacity retention. These improvements have been attributed to several factors including lowering the charge transfer resistance, increasing lithium ion diffusion coefficient, increasing the electronic conductivity, inhibiting side reactions between electrolyte and cathode material, and suppressing TMD.[31–35] Graphene, a highly crystalline allotrope of carbon, is desirable for its outstanding electrical, thermal, and mechanical properties.[36] For all the coating materials mentioned above, the particular method of applying the coating is a key factor to its success, and graphene coatings, in particular, present challenges.

Bottom-up techniques have been widely used to apply coatings to CAM. Generally speaking, these involve the deposition of atoms and or molecules from solution or vapor directly onto the cathode material to form a coating or thin film; the coated material may or may not need to undergo subsequent processing, e.g. annealing, to achieve a desired film microstructure. There are several bottom-up methods, and they can be broadly classified as "wet" or "dry".

---

[z] E-mail: daboyd@caltech.edu

Respective examples include solution deposition of sucrose, and subsequent annealing, to form a carbon coating on $LiNi_{0.5}Mn_{1.5}O_4$[37] and atomic layer deposition (ALD) of Al_2O_3 on $LiNi_{0.5-x}Mn_{1.5+x}O_4$ (LNMO).[38] Although bottom-up methods have been useful to demonstrate the efficacy of many types of coatings, there are challenges in practical implementation.[39] Graphene, for example, is only known to form on limited materials and under conditions that may damage the underlying cathode material.[40]

An alternative coating method is "dry coating", aka mechanofusion, dry particle fusion, high-intensity mixing, or ordered mixing.[41,42] Dry coating avoids the need for solvents, high temperature, and vacuum, making it amenable to a variety of coatings and CAM, and it is also a scalable process that has been used in industrial applications since the 1980s, including pharmaceuticals, toners, lubricants, and cosmetics.[43] Dry coating is a top-down approach, wherein previously formed "guest particles" are attached to relatively much larger "host particles" using mechanical forces.[44,45] Dry coating of cathodes is an emerging application, and the earliest report is of TiO_2 guest nanoparticles (<100 nm) coated onto $LiCoO_2$ (LCO) host microparticles (20 μm).[46] Dry coatings of oxides,[46–50] carbons,[51,52] and nano-composites of oxides and carbons[53] have since been demonstrated with range cathode materials including LCO, NMC, NCA,$Ni(OH)_2$, and LNMC, showing similar improvements in charge capacity and or in capacity retention as their bottom-up counterparts.

However, the efficacy of dry coatings in suppressing TMD is an open question. Although dry coatings have demonstrated improved performance, this can be for several reasons including suppression of TMD. Son et al. dry-coated $LiNi_{0.6}Mn_{0.3}Co_{0.1}O_2$ (NMC631), a Ni-rich CAM, with a graphene-silica nanocomposite, called "graphene balls", and demonstrated relative improvements in rate capability and capacity retention.[53] However, NMC631 is not known to be subject to appreciable TMD. Dry coating does not necessarily form impermeable layers, which is believed to be necessary to protect the CAM from TMD. To the best of our knowledge, suppression of TMD by dry coatings has not yet been demonstrated.

In this work, we compare the performance of NMC811 and LNMC (half-cells) with and without coatings of graphene-encapsulated nanoparticles (GEN). The GEN comprise silica nanoparticles (10–20 nm) coated with graphene produced by microwave plasma-enhanced chemical vapor deposition (MW-PECVD) in a fluidized bed reactor (FBR). MW-PECVD, an alternative to thermal CVD which was used by Son, et al. is capable of producing very high quality graphene at lower temperatures.[54] NMC811 is also a Ni-rich CAM, and cells with GEN dry coatings (NMC811-GEN) showed relative improvements in rate capability similar to those reported by Son et al. at 25 and 60 °C in NCM613. The LNMC cells with GEN dry coatings (LNMC-GEN) demonstrated improvements in both cycle life and rate capability. LNMC is known to suffer from TMD. Inductively-Coupled Mass Spectrometry (ICP-MS) was used to measure the transition metals in the lithium foil anodes of LNMC cells that were cycled to upper cutoff voltages (UCV) of 4.30, 4.45, and 4.60 V, at 60 °C. It was found that the dry coatings of GEN coatings suppressed the concentration of Mn, Ni, and Co dissolved from the cathode and subsequently reduced at the anode at all UCV. These results conclusively demonstrate that dry coatings of GEN can suppress TMD.

Experimental

PECVD.—GEN were prepared by microwave PECVD in a quartz fluidized bed reactor (FBR).[54,55] Silica nanopowder (10–20 nm), purity 99.5% on trace metals analysis (Sigma-Aldrich, 637238) was used as the starting material. The nanopowder was placed in the FBR and baked at reduced pressure (500 mTorr) under flowing Ar at 125 °C for two hours prior to PECVD growth to remove moisture. The PECVD process gasses were H_2 and CH_4, and the process pressure was 750 mTorr. The gas flows were controlled at a ratio of H_2:CH_4 (5:1.2) and the magnitude of the flows depended on the degree of fluidization required and were typically on the order 1-10 sccm. The microwave power used during PECVD growth was $\sim$100 W. The growth time depended on the amount of silica in the tube and would typically be a few hours for several hundred mg of material. Pristine SiO_2 is snow white, and PECVD process was stopped when the powder became uniformly black, Fig. S1. Separate batches of GEN were created for NMC811 and LNMC, and the carbon content, as measured by TGA, was 11% and 17%, respectively. (TGA scans are provided in Fig. S2.) Further details of the PECVD system and growth can be found in the Supplemental Information (SI)).

TEM.—Bright field images were obtained using a Thermo-Fischer TF30 transmission electron microscope operated at 300 keV. Particles for imaging were suspended in propanol and deposited onto a holey carbon film. High resolution images were acquired with the objective aperture removed.

XRD.—Scans from 10 to 60 degrees in 2Θ angle were obtained using Cu Kα scans on a Philips PW3040-Pro diffractometer and 15 to 80 degrees in 2Θ using Cu Kα on a Rigaku Smartlab diffractometer.

TGA.—Measurements on the LNMC material were made on a NETZSCH TG 209F1 Libra TGA209F1D-0286-L. The heating atmosphere was Ar/O_2 4:1 and the ramp rate was 5 °C/min in an alumina pan. The TGA measurements on the 811 material were made on a Shimadzu TGA-50H. The heating atmosphere was dry air and the ramp rate was 5 °C min^{-1} in a platinum pan.

XPS.—X-ray photoelectron spectroscopy (XPS) was performed using an AXIS-Supra system (Kratos Analytical Inc.) equipped with a monochromatic Al Kα source. The vacuum is maintained below 5×10^{-8} Torr during the measurements. Survey spectra were acquired using 160 eV pass energy, 100 ms dwell time and 1 eV step. Detail spectra of O 1s, C 1s were acquired using 20 eV pass energy, 0.1 eV step, 100 ms dwell time and averaged for 10 scans. A charge neutralizer was used to remove charging effect upon photoemission, and the energies of all spectra were calibrated to the main C 1s peak at 284.5 eV.

Raman spectroscopy.—A Renishaw In Via micro Raman system with Streamline^{TM} with fast mapping capabilities was used to create Raman maps of the pristine GEN and of the GEN dry-coated on to the cathode material. Renishaw Wire^{TM} software was used to both control the acquisition and perform analysis of the Raman data. The typical Raman scan parameters were as follows. A 532 nm laser (100 mW) was used with a 50X objective, and the laser power on the sample used was kept low at $\sim$10% of full power to avoid damage to the CAM. For mapping, the laser was focused through a cylindrical lens to form a line 25 × 1.5 μm. The mapping step size was typically 2.5 μm, and the exposure time was 25 s. The spectral range was 1014 points from 1279.5 to 2818.7 (cm^{-1}). Raman mapping was used to both identify the types of deposited carbon and to assess the coverage within the bulk silica powder that comprised GEN. Raman mapping involves collecting Raman spectra at pre-determined spatial intervals across the sample and then reducing each spectrum or features thereof to a representative map value. The Raman mapping data in this work was reduced using cluster analysis. Cluster analysis statistically groups similar spectra into clusters, and the resulting cluster maps provide a means to visualize and quantify the distribution of the components. The distributions of each the clusters were quantified within the Raman map the mask feature of Wire^{TM}. The effects of Cosmic rays were removed from the spectra prior to cluster analysis.

Dry coating.—Dry coating was performed using a Nobilta Nob-mini (Hosokawa Micron Corporation) high-intensity shear mixer. Prior to shear mixing, the cathode materials and the GEN (1 wt%)

were mixed together with a mortar and pestle. For each cathode material, NMC811 and LNMC, six coating runs were performed: two batches with uncoated nanoparticle SiO_2 and four batches with GEN. A range of mixing times (min) and blade speed (rpm) were used. Raman mapping of the mixed materials was used to select the batches for the cells. The NMC811 material (MTI Corporation) was mixed with at 3000 RPM for 5 min, and the LNMC material (NEI Corporation) was mixed at 9000 RPM for 10 min.

Coin cell preparation.—The active cathode materials used were: LNMC, NEI Corporation and NMC811, MTI Corporation. The cells used throughout this study were 2032 size cells in half-cell configuration. In each batch of cells, there were typically four control cells with standard active cathode material (CAM) and four cells with GEN coating (1 wt%) on the CAM. The compositions of the half-cells were as follows. Control cells CAM (87%), Shawinigan black (6%), and PVDF (7%). Graphene cells: CAM with 1 wt% GEN (87%), Shawinigan black (6%), and PVDF (7%). The build values for LNMC are as follows: the active mass, 14-15 mg; the total mass, 35 mg; the electrode area, 2 cm^2; and the loading, 9 $mg\,cm^{-12}$. The build values for NMC811 are follows: the active mass, 18 mg; the total mass, 38 mg; the electrode area, 2 cm^2; and the loading, 11 $mg\,cm^{-12}$. The anode consisted of two layers of lithium foil. The electrolyte was 1.0M $LiPF_6$ in EC+EMC(30:70). The separator was polyethylene (Tonen). All cathodes were stored overnight in a 100 °C vacuum oven. The cells were assembled in a battery dry room then the filled with electrolyte and sealed in an argon-filled glove box (water content <1 ppm).

Cycling.—The cycling measurements were performed either using a Novonix (CMA-HDX-99-56) or a Maccor 2400. The Novonix system was equipped with a 16 position environmental chamber, while the cells cycled with the Maccor test station were cycled in a Tenney (TUJR) environmental chamber. Cells were allowed to thermally equilibrate for two hours before cycling. Cells were formed at 25 °C for five cycles with the following protocol: CC charge at C/20 to upper cutoff voltage (UCV); hold CV at UCV for one hour; rest for 15 min; discharge CC at C/20 to 3.0 V; and rest for 15 min. Cycling of the LNMC and NMC811 half-cells used the following protocol: CC–CV charge to the UCV and hold at UCV until current tapers to C/10; rest 15 min; CC discharge at CC to 3.0 V; rest 15 min; and repeat.

Cycling with EIS.—Electrochemical impedance spectroscopy (EIS) (potentiostatic) was performed throughout some cycling measurements using a Bio-Logic SP-150e dual channel potentiostat. The spectrum collection amplitude was 10 mV from 1 MHz to 10 mHz. There were 6 points per decade in logarithmic spacing and drift correction was applied. Spectra were collected at top-of-charge after a 15 min rest period after the first charge and then after every third cycle. The control and coated cells were cycled simultaneously inside a Tenney (Model TUJR) temperature test chamber. Cells were discharged at a rate of 1C (CC) to 3.0 V and then charged at a rate of 1C (CC–CV), to either 4.30, 4.45, or 4.45 V, then rested for 15 minutes before discharging.

ICP-MS.—Inductively Coupled Plasma- Mass Spectrometry (ICP-MS) was performed on lithium foil anodes. After the cycling was complete, the cells were discharged to 3.0 V and held for 1 hour, and this process was repeated as needed to ensure that all the cells were at the same OCV. The cells were dissembled in a battery dryroom. The lithium foil anodes from the cycled cells were rinsed in neat ethyl methyl carbonate (EMC) and allowed to air dry in the dryroom to remove any residual electrolyte salt. After rinsing, the lithium foil anodes were stored in the dryroom until commencing the ICP-MS tests. Two reference anodes were prepared. The first was a pristine lithium foil, and the second was an identical foil that was assembled into a 2032 coin cell with a cathode, separator, and electrolyte as a control but not cycled. All the anodes were weighed, placed into 50 ml vials, and then allowed to sit in air for several days to slowly oxidize, preventing any violent reaction and subsequent aerosolization of the lithium upon being subjected to the strong, aqueous acids used in the digestion process. Concentrated HCl, 500 μl, was added to each vial followed by 500 μl of concentrated HNO_3. The vials were heated using a block heater to 95 °C and refluxed for 4 hours after which point the samples were dry. Upon cooling 5% wt/vol HNO_3 (5%) was added to each Digitube vial (SCP Science) to reach a final volume of 50.0 ml.

Nickel, cobalt and manganese concentrations were measured with an Agilent 8800 ICP-MS. The sample introduction system consisted of a micromist nebulizer, Scott-type spray chamber and fixed injector quartz torch. A guard electrode was used and the plasma was operated at 1500 W. Elements were determined in no-gas single-quad mode. Standards were prepared from a ICP-MS standard mix of first row transition elements (CCS—6, Inorganic Ventures, Christiansburg, VA, USA) in the range of 0 to 40 μmg/L of each element. The standards were matrix matched to the samples by addition of lithium to 200 mg/L using a single element ICP-MS standard stock (PlasmaCAL, SCP Science, Champlain, NY). Detection limits and background equivalent concentrations (BEC) for all elements were below 10 ng/l with the exception of the BEL for Mn which was 25 ng/L. The probe was subjected to 4 rinses (1 flowing, 3 static) between samples to minimize any possibility of cross contamination. Sample to sample carryover was verified to be less than 1% between the highest standard and the blank. Results were analyzed using ICP Masshunter 4.5 (Agilent Technologies). The Agilent 8800 ICP-MS at the Resnick Sustainability Institute's Water and Environment Lab at the California Institute of Technology was used in this work.

Results and Discussion

Synthesis of GEN and microstructure.—GEN were prepared by microwave PECVD in a quartz fluidized bed reactor (FBR).[54,55] The process involved exposing silica nanopowder (10–20 nm) to a cold plasma of H_2 and CH_4.[54,56] The PECVD process is notably different than thermal CVD, which was used by Son et al. to produce graphene balls.[53] Thermal CVD of graphene occurs by the catalytic dehydrogenation of methane on the substrate. It is an atmospheric, high temperature process, e.g. 1000 °C, and being catalytic, the growth is self-limited once the substrate is covered with carbon. In the case of graphene balls, catalysis is a result of reducing the underlying SiO_2 nanoparticles. In contrast, PECVD growth occurs by active species generated in a low-pressure plasma. It is catalyst-free and growth is not limited by access to the substrate, which can allow for extended multilayer graphene sheets to form. The methane-hydrogen plasma is a rich chemical environment that can simultaneously support a variety of active species. Carbon deposition is predominantly by methyl radicals, and atomic hydrogen can etch amorphous carbon, resulting in formation of highly crystalline carbon.[57] Atmospheric species can also be present in the plasma e.g. ozone and atomic oxygen, which for example can allow for the inclusion of oxygen functional groups. The growth temperature can also be much lower, e.g. 425 °C,[54] which can allow functional groups to remain in the graphene.

The PECVD growth conditions for GEN are similar to those of vertical graphene (VG), which uses relatively higher flows of CH_4 than for planar graphene.[58–60] VG growth is a single-step process that occurs in two stages, Fig. 1a. The first stage is the formation of a basal (buffer) layer on the substrate. This layer is typically either nanographitic or amorphous carbon in nature with a thickness of (10–20) nm. The second stage is the emergence of VG from the base layer. It is generally believed that this occurs as a result of a planar mismatch of adjoining graphite layers and from areas of high curvature [61] In the case of GEN, the particles are first coated with a layer of crystalline carbon and the inherent high curvature of the silica nanoparticles, and the associated high film stress, presumably promotes the emergence of VG.[62]

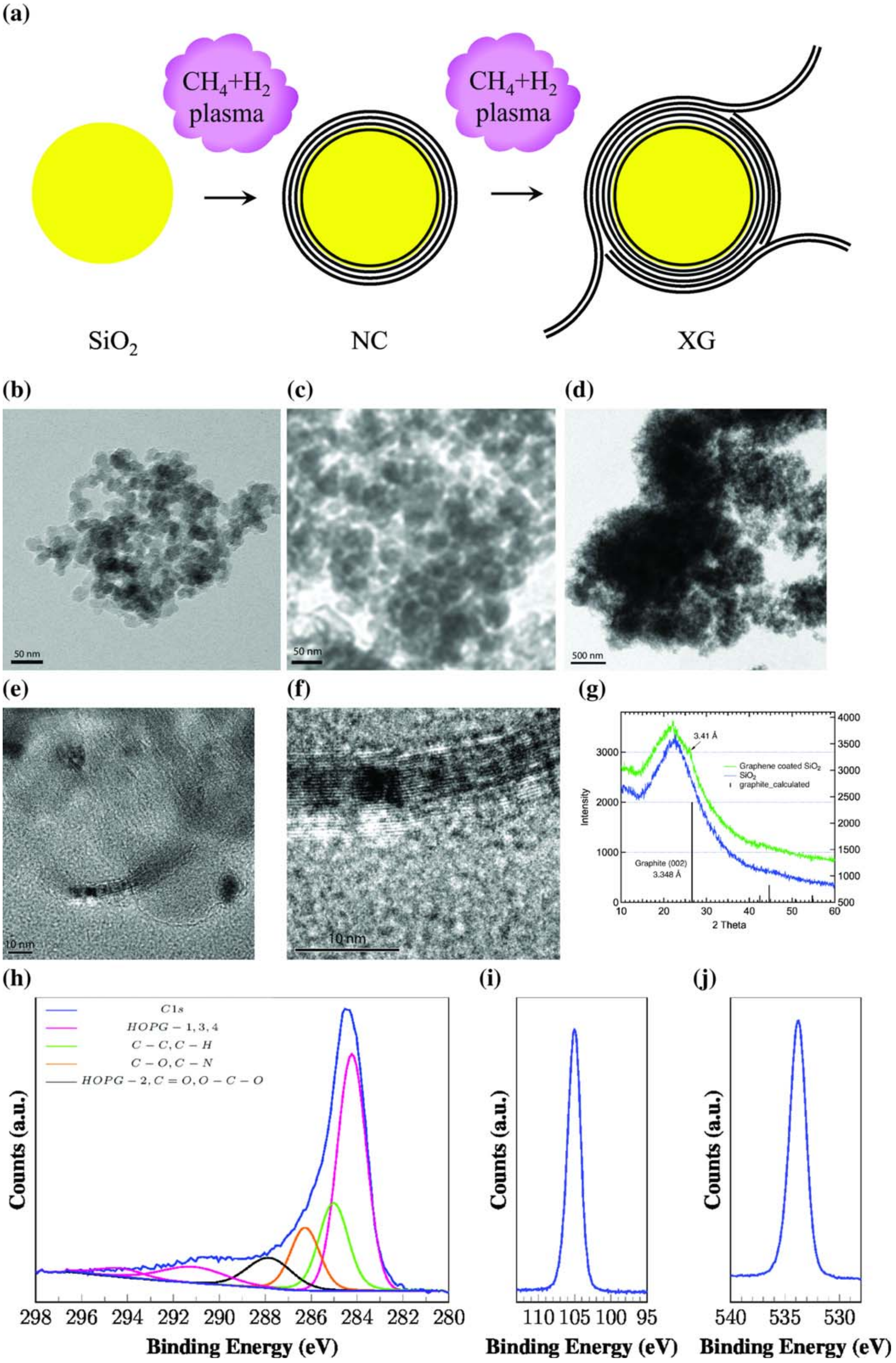

Figure 1. GEN Synthesis and Microstructure. (a) Schematic of GEN PECVD process, left to right. Nanoparticles of SiO_2 are exposed to a cold plasma of CH_4 and H_2 forming a layer of nanocarbon (NC). With continued exposure to the plasma, extended graphene (XG) forms. (b)–(f) TEM images of (b) pristine (as-received) nanoparticle SiO_2, scale = 50 nm, (c) nanocarbon (NC), scale = 50 nm (d) extended graphene (XG),scale = 500 nm, and (e)–(f) layered graphene, scale = 10 nm. (g) XRD of pristine GEN and (as-received) nanoparticle SiO_2. (h)–(j) Detailed regions of the XPS spectrum for the pristine GEN: (h) C1s (i) Si2p, and (j) O1s.

TEM and Raman mapping provide complementary evidence to support this growth mechanism. Given the stochastic nature of the FBR it is reasonable to assume that within the pristine GEN there are different stages of growth present. For example, we would expect to have a mixture of carbon coated silica particles with and without extended graphene sheets. Shown in Figs. 1c–1f are TEM images of pristine GEN. Figure 1d, is a low magnification image showing an agglomeration of GEN highlighting both the extended graphene

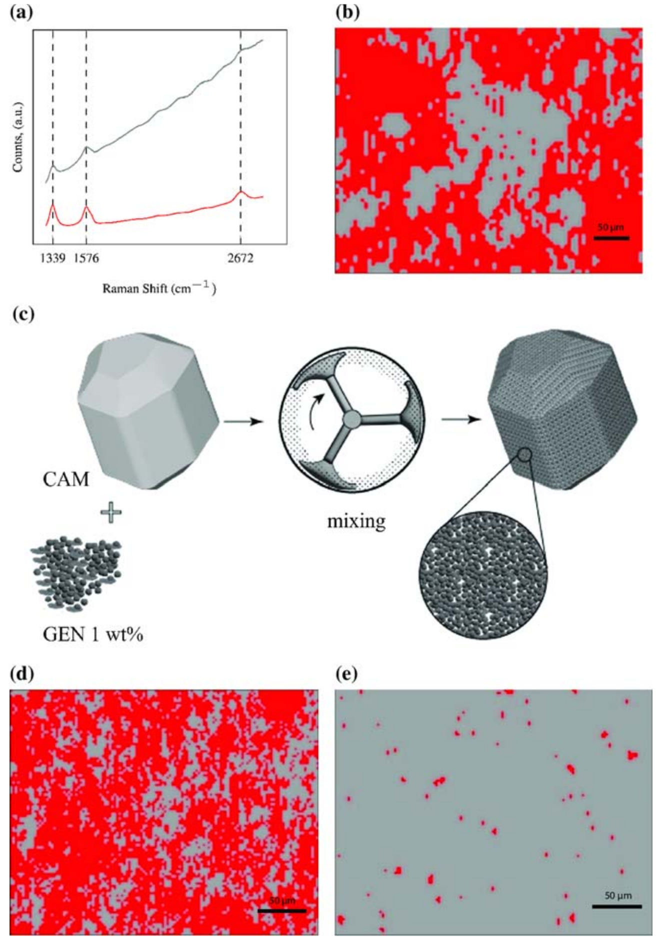

Figure 2. Microstructure and Coverage of GEN Dry Coatings. (a) Component spectra derived from RMCA of pristine GEN. The red spectrum (bottom) is extended graphene (XG), and the gray spectrum (top) is nanocarbon (NC). The colors of the spectra correspond to the component colors in the subsequent maps. (b) Raman component map of pristine GEN, scale = 50 μm. (c) Schematic of the dry coating process, left to right. CAM and pristine GEN, 1 wt%, undergo mixing, coating the CAM. (d)-(e) Raman component maps of CAM dry coated with GEN (d) NMC811-GEN and (e) LNMC-GEN, scale = 50 μm.

sheets and the coated nanoparticles. Figures 1e and 1f are a higher resolution image showing the presence of layered graphene structures. Figure 1c shows a region of nanoparticles on which carbon is deposited but extended graphene sheets have not yet formed. For comparison, Fig. 1b is a TEM image of "pristine" (as-received) SiO_2 nanoparticles. The average diameter of the pristine particles is approximately 21 nm and that of the carbon coated particles is 37 nm, which is a layer thickness of 8 nm.

Raman spectroscopy is considered the "gold standard" for identifying graphene and other allotropes of carbon. Raman mapping cluster analysis (RMCA) of the pristine GEN produced two representative component spectra, which are shown in Fig. 2a. The red (bottom) spectrum has features at 1339, 1576, and 2672 cm^{-1}, which are characteristic of the D, G, and 2D peaks of graphene, respectively. The D/G, 2D/G ratios, and the slight shoulder on the G peak is consistent with mulitilayer, vertical PECVD graphene.[60,63] The gray (top) spectrum is similar to the first but has only weak D and G peaks, indicating that it is carbon, but not necessarily graphene. These D and G peaks are distinct and do not overlap suggesting that the carbon is not amorphous. This layer is ascribed as nanocarbon (NC).

Comparing the TEM images with the RMCA, the extended carbon sheets in 1d are ascribed to extended graphene (XG) and the carbon coating on the silica particles is ascribed to NC, Fig. 1c. Furthermore we associate the NC layer with the PECVD basal layer. Although the Raman spectrum of NC component is not strictly that of graphite, the basal layer is constrained by the underlying nanoparticle, and surface constraints may affect local density of states.[64] Also, it is known that there are changes in the Raman spectrum of graphite at nanometer crystallite scale.[65] Figure 1f shows layered structures on the order of 10 nm. The curvature of these structures suggests that they are associated with a nanoparticle coating. The thickness of this coating is consistent with the average measured thickness of the NC, 8 nm, and the layer spacing is consistent with graphite.

X-ray diffraction (XRD) (Cu Kα) scans of the (pristine) GEN Fig. 1g shows a small shift toward larger spacing of the GEN peak (position noted by the arrow) indicating a 3.41 Å spacing in comparison to the 3.348 Å spacing expected from graphite. This slightly larger lattice spacing of the GEN is consistent with the high magnification image of the graphene layers, Fig. 1f, which is somewhat less coherent than might be expected from a *c*-axis projection of graphite. XRD scans of pristine nanoparticle SiO_2 are provided for comparison (lower trace).

X-ray photoelectron spectroscopy (XPS) was used to examine the elemental composition and the chemical and electronic states of the GEN. The primary elemental components present in the four survey spectra, not shown, were Si, O, and C, along with a trace amounts of N. Using the calibrated sensitivity factors, S_i, for this instrument and assuming equivalent homogeneous compositions, the average relative at% of Si, O, and C, were 18.9 ± 0.3, 46.0 ± 1.5, and 34.7 ± 1.9%, respectively. Trace amounts of Na and F were also observed, and these are associated with impurities in the SiO_2 nanoparticles and with the vacuum pump oil used in the PECVD system, respectively. High resolution XPS spectra of pristine GEN are shown in Figs. 1h–1i. The representative C 1s region is shown in Fig. 1h. Given the predominance of defective graphene present in the Raman spectra, the C1 s regions were fit following the procedure of Gengenbach et al. which starts with a fit to purely graphitic carbon (highly oriented pyrolytic graphite (HOPG)) and then adds functional components based on the elements present in the survey spectra and in the process conditions.[66,67] This approach is consistent the characterization of defective graphene wherein the D-band present in the Raman spectra is non-specific and can include not only structural defects, e.g., edges, but functional groups as well. The resulting C 1s components are shown in Fig. 1h; binding energies (BEs) and FWHMs of these components were constrained based on literature values.[66] There are four peaks associated with graphene. The asymmetric peak at 284.2 eV is the graphitic feature, and the higher energy features at 287.7, 291.0, and 294.2 eV are the associated shake-up peaks. These peaks are labeled HOPG-1,2,3,4, respectively, Fig. 1h. The component at 285.0 eV is associated with both C–C and C–H. The component at 286.3 eV is associated with both C–O and C–N. The component at 287.9 eV is associated with both C=O and O–C–O. The amount of nitrogen present in the survey spectra was negligible, and we can assume the same for C-N bonds. There is no evidence of SiC, 282 eV. An exact quantification of this C 1s spectra is challenging because the overlap of the HOPG-2 (287.7 eV) and the C=O and O–C–O (287.9 eV) is beyond the energy resolution of this instrument, 0.4 eV. Furthermore, the areas of these individual peaks were found to be roughly equivalent. The HOPG-2 and the C=0 and O–C–O components were combined into a single feature in Fig. 1h. The sp^2/sp^3 ratio of the GEN was determined by analysis of the C (KLL) Auger peak in the survey spectra using the D-value method.[68] The average $\%sp^2$ from four survey scans is 60% ± 10%, (D-value = 19.3±0.9). This value is in the range of hydrogenated carbons and is consistent with the feature at 285.0 eV, which is partially associated with C-H. (For comparison, the D-value of HOPG, which is 100% sp^2, is 22.5). The presence of C–H in the C 1s spectrum is consistent with the PECVD environment of CH_4 and H_2. The Si 2p region is shown in Fig. 1i. The region extends from 101 to 108 eV and is centered at 104.9 eV.

There is no evidence of elemental Si, 100.5 eV. The region is ascribed to nanoparticle silica.[69–71] The O 1s region is shown in Fig. 1j. It is centered at 534.0 eV and extends from 531 to 528 eV. An accurate fitting of the region is challenging because of the contributions from the C-O functional groups in the carbon and the underlying SiO_2.[72] We note that the BE for O 1s SiO_x $(0 < x < 2)$ are lower than 532.8 eV. Taken together, the C 1s, Si 2P, and O 1s features indicate that silica nanoparticles have not been reduced or have formed SiC during the PECVD process. The ratio of Si:O taken from the survey scan is 1.0:2.4 compared to 1.0:2.0 for stoichiometric SiO_2. This excess of oxygen, 8%, is consistent with the analysis of the C 1s region, which indicates the presence of C-O. Oxygen groups in the GEN are presumably the result of reactive plasma species formed concurrently during growth from residual air present in the PECVD system, Fig. S2.

Microstructure and coverage of GEN dry coatings.—The dry coating process is illustrated in Fig. 2c. CAM and pristine GEN, 1 wt %, undergo mixing, coating the CAM. Dry coating can be affected by a number of factors including the relative sizes of the host and guest particles and bulk density of the host powder, and the optimal run time and blade speed for each CAM were determined empirically. RMCA was employed to assess the distribution of XG and NC within the pristine GEN and the dry-coated CAM. RMCA show a difference in the relative amounts of XG and NC before and after dry coating. The ratio of XG:NC in the pristine GEN used with NMC811 was found to be 93:7, and upon dry coating onto the NCM811 the ratio was 50:50, Fig. 2d. The ratio of XG:NC in the pristine GEN used with LNMC was 79:21, Fig. 2b, and upon dry coating onto the LNMC the ratio was 1:99, Fig. 2e.

This disparity in the ratios of XG:NC in the NMC811-GEN and LNMC-GEN can by understood by comparing the microstructure of the pristine GEN with that of the CAMs. Dry coating is inherently affected by the relative sizes of the guest and host particles, and it is assumed that the guest particles are at least 10 times smaller than the host particles[44] From the discussion above, we see that the pristine GEN is a mixture of XG and NC structures, which have very different sizes. The GEN-NC structures have characteristic sizes of 38 nm and the GEN-XG can extend up to hundreds of nanometers. In comparison, the average particle size of the NCM811 is $D_{50} = 9 \sim 15\ \mu m$, per the supplier. This is supported by SEM images of pristine NMC811 powder, Fig. S4, showing that it comprises mainly secondary particles on order of 10 μm in diameter. These particles are much larger than either the GEN-NC or the GEN-XG, and as such both the GEN-NC and GEN-XG should be able to effectively dry-coat the NMC811. However the microstructure of LNMC is much different. SEM images of the LNMC-GEN after dry coating, Fig. S5, show that the LNMC consists mainly of primary particles with an average diameter of 200 nm. This size is on the order of the GEN-XG, and as such, it would not be expected that the GEN-XG would effectively coat the LNMC. On the other hand, the primary particle size of the LNMC is 5X larger than the GEN-NC. Although this size difference is not considered not ideal, it is sufficient to allow the GEN-NC to coat the LNMC primary. These results highlight the importance of understanding the relative microstructure for dry coating.

Cell-level testing.— *NMC811.*—The comparative effects of GEN coatings on the rate capability of NMC811 at 25 and 60 °C are shown in Figs. 3a and 3b. Four NMC811 and four NMC11-GEN cells were cycled simultaneously. Each cell was charged and discharged for three cycles in a stepped progression of charge rates, C/10, C/3, C/2, 1C, 2C, and 5C (1C ≡ 180 mA g^{-1}). The discharge capacities of NMC811 and NMC811-GEN at 25 and 60 °C, are shown in Figs. 3a and 3b, respectively. The averages for each step are summarized in Table S1. At 25 °C, there are slight increases in the rate capabilities of GEN cells at C/10, C/3, C/2, and 1C, of 6, 6, 7, and 6% respectively, and no significant differences between the control and GEN cells at 2C and 5C. However at 60 °C, the differences are significant. The NMC811-GEN cells exhibit higher rate capabilities at all charge rates. At C/10, C/3, C/2, C, 2C, and 5C at the relative differences are 10, 13, 17, 19, 21, and 23%, respectively. The cycling performances of the NMC811 half-cells from 3.0 to 4.3 V at 25 and 60 °C are shown in Fig. S6. At 25 °C, both the coated and uncoated groups of cells suffered severe capacity loss before 80 cycles, and at 60 °C, similar behavior was observed even before 20 cycles. ICP-MS measurements were performed on a pair of these NMC811 cells and no evidence of TMD was found in either the NCM811 or NMC811-GEN cells.

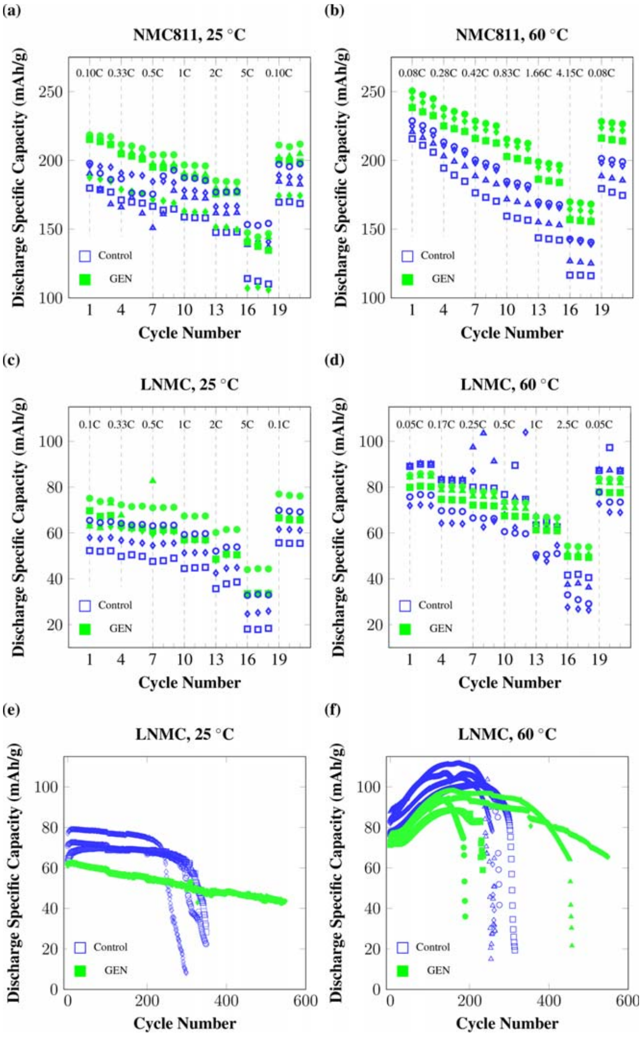

Figure 3. Improvements in rate capabilities and cycle life. (a)–(b) NMC811 rate capabilities (1C ≡180 mAh/g, 3.0-4.3 V) at (a) 25 °C and (b) 60 °C. (d-c) LNMC rate capabilities (1C ≡150 mAh/g, 3.0-4.3 V) at (c) 25 °C and (d) 60 °C. (e-f) LNMC cycling performance at 1C, (e) 25 °C and (f) 60 °C. (NMC811-GEN, LNMC-GEN: closed, green markers; NMC811,LNMC: open, blue markers.)

LNMC.—Shown in Figs. 3c–3g are the comparative effects of GEN coatings on rate capability and cycling performance of LNMC. Figure 3c is a comparison of rate capabilities at 25 °C. There were three LNMC cells and four LNMC-GEN cells. Each cell was charged and discharged for three cycles in a stepped progression of increasing charge rates, C/10, C/3, C/2, C, 2C, and 5C, (1C ≡150 mA/g, 3 to 4.3 V). The graphene cells exhibited, on average, higher charge rate capacities at all charge rates. At C/10, C/3, C/2, 1C, 2C, and 5C the relative differences are 16, 15, 17, 15, 17, and 42% respectively. These rate capability results are summarized in Table S2. Shown in Figs. 3f and 3g are the cycling performances at

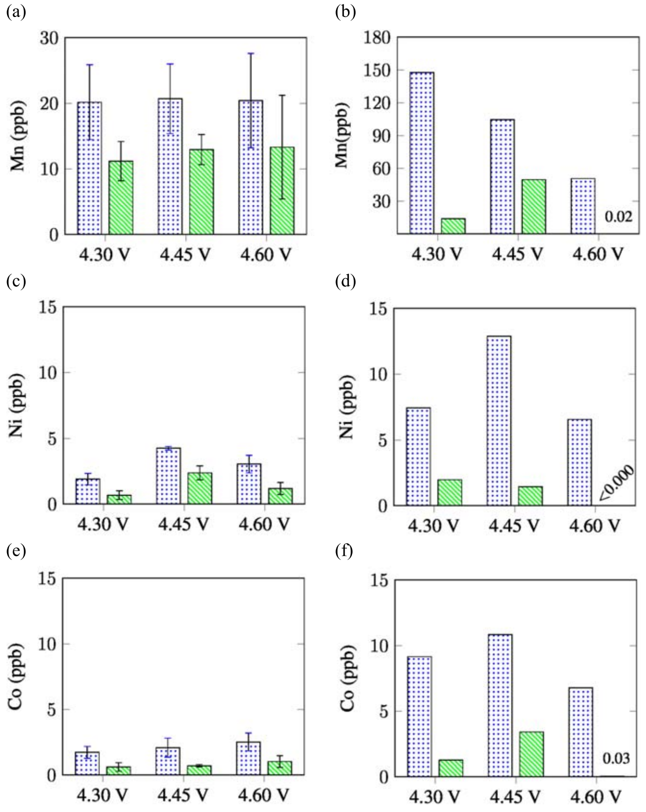

Figure 4. Suppression of TMD. Comparison of the concentrations of Mn, Ni, and Co, found in the lithium anodes of LNMC cells with and without GEN coatings after cycling (green-hatched, and blue-dots, respectively). The cells were cycled at 1C (1C ≡ 150 mA g^{-1}) , 60 °C, and between 3.0 V and UCVs of 4.30, 4.45, and 4.60 V. The left column of panels, (a), (c), (e), represents groups of eight cells that underwent limited cycling at a particular UCV and all were stopped when any one of the cells lost approximately 30% of its initial capacity. In each group there were four cells with and four without GEN coatings, and each bar represents the respective average. The right column of panels ((b), (d), (f)) represents individual cells that underwent extended cycling with EIS spectra taken every third cycle.

25 and 60 °C, at 1C, 3 to 4.3 V. In Fig. 3f there are three LNMC cells and two LNMC-GEN cells. (All graphene cells had similar capacity values and their cycle life curves overlay each other.) The cell lifetimes with and without the GEN coatings are remarkably different. The LNMC cells failed abruptly between 300 and 400 cycles, while both LNMC-GEN cells cycled past 550 cycles. Similar behavior is observed at 60 °C. In Fig. 3g there are four LNMC cells and four LNMC-GEN cells. The control cells all fail around 300 cycles. The behavior differs for the LNMC-GEN cells. One cell fails at 200 cycles; one cell began to exhibit erratic behavior at 250 cycles; and the other two cells cycled beyond 450 cycles. Shown in the Fig. S7b is this same data overlaid with GEN that was mixed (1 wt%) with the conventional mixing rather than dry coating. These cells perform similarly to the control cells, indicating the effectiveness of the dry coating in improving the cell lifetimes. This also indicates that the increase in cell lifetimes is not solely due to the desiccative nature of the SiO_2 particles and that the combination of graphene and SiO_2 improves performance and dry coating. Shown in Fig. S7a are the rate capabilities of LNMC cells dry-coated with pristine SiO_2 (20 nm) at 25 °C. For comparison this data is overlaid with the data in Fig. 3c. The cells dry-coated with pristine SiO_2 have comparatively reduced rate capabilities at all charge rates.

TMD studies.—We performed a systematic study of TMD in LNMC over a range of upper cutoff voltages (UCV) of 4.30, 4.45, and 4.6 V. At each UCV, groups of four control cells and four cells with GEN coatings were simultaneously cycled at 1C (150 mA/g), 60 °C. These cells underwent *limited* cycling, i.e. until all the cells had undergone at least 8 cycles and one of the cells in the entire group had lost at least 30% capacity. These cycling results are shown in Fig. S8. We also performed a separate cycling study involving EIS. At each UCV, pairs of cells, one control cell and one GEN cell, were simultaneously cycled while performing EIS every third cycle at 1C, 60 °C. These cells underwent *extended* cycling, i.e. they were cycled continuously until suffering dramatic losses in capacity. The two cells at each UCV were cycled for similar times. These cycling results are shown in Fig. S9.

The lithium anodes from all of these LNMC cells were harvested and studied by ICP-MS. Shown in Fig. 4 are comparisons of the concentrations (ppb) of Mn, Ni, and Co, found in the lithium anodes from LNMC half-cells with and without GEN coatings after cycling. The left-hand column of Figs. 4, 4a, 4c, and 4e, are the concentrations (ppb) of Mn, Ni, and Co, respectively, from ICP-MS for the LNMC cells that underwent limited cycling, and the right-hand column of Figs. 4, 4b, 4d, and 4f, are the concentrations of Mn, Ni, and Co, respectively, for the LNMC cells that underwent extended cycling and EIS. The results for the control, uncoated, cells at a given UCV are shown in blue, dotted, bars, and the results for the GEN coated cells at a given UCV are shown in green, hatched bars. The TM concentrations in the left hand column are the average of the four cells that underwent limited cycling at a particular UCV, and the error bars are the standard error (SE). The TM concentrations in the right hand column are the measured values for the pairs of cells at a given UCV that underwent extended cycling and EIS.

Overall, the concentrations of Mn, Ni, and Co at all the UCV were significantly higher in the anodes of the uncoated cells than the in coated cells for both limited and extended cycling. This clearly shows that the GEN coatings are effectively suppressing TMD over a range of UCV. The TM concentration levels were higher for the uncoated cells that had undergone extensive cycling than limited cycling. For both groups of cells, Mn was the most prevalent transition metal followed by Ni and Co. The Mn concentrations for cells that underwent limited cycling was nearly constant with UCV: 20 ppb for the uncoated cells and 12 ppb for the coated cells, Fig. 4a. The Mn concentrations for the cells that underwent extended cycling varied with UCV. At 4.30, 4.45, and 4.60 V, the concentrations were approximately 148, 105, and 51 ppb, respectively, for the uncoated cells and 14, 50, and 0.02 ppb, respectively, for the coated cells, Fig. 4b. Summaries of the ICP-MS results for the cells that underwent limited and extended cycling are provided in Table S3 and Table S4, respectively.

The final EIS spectra at each UCV are shown Fig. S9. Overall, there is lower resistance in the graphene cells indicating reduced charge transfer. Comparison of EIS mid-frequency intercepts, Z'_0, with cycling and UCV is shown in Fig. S10. Analysis of the Warburg tail region generally shows improved Li^+ diffusivity for LNMC-GEN, Fig. S11.[73,74]

XRD scans of both LNMC and LNMC-GEN cathodes after cycling at 4.6 V at 60 °C are shown in the Fig. S12. Of note is the greater intensity of planes in the direction of the *c*-axis of the milled cathode (both (003) and (104) planes) whereas (101) and (110) planes have intensities that are comparable in both the control and milled cathode, suggesting that the crystallographic structure of the cathode is better retained during cycling in the milled material.

Overall, these improvements in rate capacity of the NMC811 are comparable with the results of Son et al. who used dry coatings of graphene balls on NMC631[53] The carbon loading of the graphene balls was much higher at 42.5%, while the carbon loading of the GEN was 11%. Both studies see improvements in rate capability with the graphene coatings compared to the control at 25 and 60 °C. The absolute capacity values for the coated materials were similar, but the pristine values of NMC631 for Son et al. were lower. There were differences in the cycling conditions. Son et al. used a lower depth of discharge 2.5 vs 3.0 V, and a higher mass loading 25 mg cm^{-2}, vs 11 mg cm^2 used in our study. Neither NMC831 or NCM811 are known to undergo appreciable TMD, and the improvements in performance can be attributed to the improved electronic conductivity provide by the graphene.

The ability of GEN dry coatings to suppress TMD *during cycling* is consistent with reports of carbon films derived from bottom-up methods.[35,75] It is believed that TMD occurs at the bottom of discharge when the concentration of Mn^{3+} is at the highest level and undergoes the following disproportionation reaction:

$$2Mn^{3+}_{solid} \rightarrow Mn^{4+}_{solid} + Mn^{2+}_{solution}$$

TMD is a complicated process involving JTD and surface reconstruction, as well as corrosion by acid (HF) generated by side reactions in the electrolyte[17,76] Furthermore, the UCV can affect which dissolution mechanism is dominant.[17] (We note that are number of studies involving corrosion tests of *uncycled* CAM[27,34,53]). Although coating the CAM with a *continuous* thin film of carbon has been shown to be effective in suppressing TMD, there is no consensus as to whether the film is preventing the disproportionation reaction or preventing Mn^{2+} from entering the electrolyte. Ghosh et al. used a coating of soft carbon (5 wt%) on $LiNi_{0.5}Mn_{1.5}O_4$ (LNMO) and found improvements in cycling performance and rate capabilities.[75] Jaber et al. created thin film cells and coated the spinel-structured LMO with a sheet of monolayer graphene, which was transferred from a copper foil growth substrate.[35] The cells were cycled extensively and comparative improvements in cycling and rate capabilities were observed.[35] Although these studies demonstrated the efficacy of carbon coatings, neither coating method is easily scaled.

Suppression of TMD during cycling by a dry coating is remarkable, especially at elevated temperatures and over a range of UCV. Dry-coated films do not necessarily form a continuous, physical barrier that could prevent TM ions from dissolving into the electrolyte and HF from directly contacting the CAM. However, the graphene in the GEN coatings does contain functional groups and defects and as evidenced by Raman spectroscopy and XPS, and these could play a role in suppressing TMD. Oxygen functional groups can act as charge donors, chelating agents, and coordination complexes, which could potentially prevent the disproportionation of Mn^{3+} or trap Mn^{+} ions as well as other transition metals. For example, manganese is well-known to bond strongly with oxygen containing groups in graphene oxide.[77,78] Similarly, graphene and oxygen containing functional groups in the coating could interact with HF created in the electrolyte.[79,80] The oxygen groups are mainly the result of residual air in the PECVD system, and the relative amount of oxygen, or other dopants such as nitrogen or fluorine, could intentionally be increased or added to improve the efficacy of the coating if the functional group is the critical variable in suppressing TMD. Graphene defects are believed to trap Mn ions while allowing Li ions to pass through.[35]

Although dry coatings do not necessarily provide an impenetrable physical coating, if the spacing of the GEN coating particles is within the diffusion length of the TM ions, the TM ions could effectively be trapped. Detailed microscopic information is less available on the role of the GEN coating in suppressing TMD, but a few general observations are possible. It seems unlikely that the GEN coating alters transition metal mobility inside the active cathode material. Diffusion of transition metal ions through the bulk material to the surface depends on the transition metal concentration in the subsurface region—the diffusion is slower if the transition metal concentration is higher near the surface. It is not clear if the GEN coatings have the greatest effect by maintaining the transition metal concentration just beneath the surface of cathode particles, or through the CEI, or both. Nevertheless, a kinetic explanation of the effect of GEN coatings on transition metal diffusion out of the active cathode particles seems more promising than a thermodynamic one. It is conceivable that the GEN coating favorably reduces the concentration gradient of Mn in the cathode particles, and reduces the loss of Mn by TMD. The improved crystal quality should result in faster diffusion of the lithium ions during charge and discharge. This is supported by marked improvements in Li^{+} diffusivity with the LNMC-GEN, as found by EIS. Similarly, measurements by Jaber et al. on cycled, uncoated LMO reveal an amorphous CEI and Mn depletion region on the order of tens of nanometers, which is an appreciable fraction of the average radius of the LNMC primary particles, 100 nm.[35] Presumably, similar regions of Mn depletion would exist in the uncoated LNMC and would contribute to the reduction the Li^{+} diffusion.

Conclusions

Graphene Encapsulated Nanoparticles (GEN), prepared by microwave plasma-enhanced chemical vapor deposition (MW-PECVD), were dry coated onto particles of active cathode materials of $LiNi_{0.8}Mn_{0.1}Co_{0.1}O_2$ (NMC811) and $Li_{1.2}Ni_{0.13}Mn_{0.54}Co_{0.13}O_2$ (LNMC). With the addition of 1 wt% GEN to the cathode active material (CAM), cells of both LNMC and NMC811 showed improved rate capability and capacity retention under all test conditions. The improvements in rate capability in NMC811, a Ni-rich CAM, are consistent with the results of Son et al. who found similar improvements with dry coatings of thermally derived graphene-silica nanostructures on NMC631, also a Ni-rich CAM. Unlike NMC811, LNMC is known to suffer from severe TMD, and it is shown here that dry coatings of GEN suppress transition metal dissolution (TMD) in LNMC and improve performance, even under stressful conditions of elevated temperature, high voltage and extended cycling. Within GEN there is a distribution of the microstructure between NC and XG, and this has proven to be useful for coating CAM particles of differing size. For example, despite not being to coat the LNMC particles with XG, the NC were effective in suppressing TMD while improving the charge-rate capacity, by up to 42% and doubling the lifetimes. GEN dry coatings offer performance improvements comparable to bottom-up carbon coatings and can be applied with a scalable, industrial process. Our results suggest that defects and functional groups present in the GEN play a role in suppressing TMD and that the GEN coatings could be further optimized. The ability of dry coatings to suppress TMD in Mn-rich CAMs may provide a path to an alternative CAM with less cobalt.

Acknowledgments

This work was supported by gifts from Lewis & Diane van Amerongen and Charles Fairchild. Key equipment was provided by GraphEnergy, Inc.

Research carried out at the Jet Propulsion Laboratory, California Institute of Technology, was under a contract with the National Aeronautics and Space Administration (80NM0018D0004).

This project benefited from the use of ICPMS instrumentation made available by the Resnick Sustainability Institute's Water and Environment Lab at the California Institute of Technology and assistance from Dr. Nathan Dalleska.

The authors acknowledge the use of facilities and instrumentation at the UC Irvine Materials Research Institute (IMRI), which is supported in part by the National Science Foundation through the UC Irvine Materials Research Science and Engineering Center (DMR-2011967). XPS work was performed using instrumentation funded in part by the National Science Foundation Major Research Instrumentation Program under grant no. CHE-1338173.

We acknowledge Ruoqian Lin and Frederick C. Krause, both formerly of JPL, and Joel Chacko, Caltech, for their contributions to this work.

ORCID

David A. Boyd https://orcid.org/0009-0009-5395-1233
Cullen M. Quine https://orcid.org/0000-0002-7301-0969

Channing Ahn https://orcid.org/0000-0003-3038-6509
William C. West https://orcid.org/0000-0001-6417-8930
Brent Fultz https://orcid.org/0000-0002-6364-8782

References

1. T. Zou, M. Khaloei, and D. MacKenzie, "Effects of charging infrastructure characteristics on electric vehicle preferences of new and used car buyers in the United States." *Transportation Research Record*, **2674**, 165 (2020).
2. W. Li, B. Song, and A. Manthiram, "High-voltage positive electrode materials for lithium-ion batteries." *Chem. Soc. Rev.*, **46**, 3006 (2017).
3. C. Xu, Q. Dai, L. Gaines, M. Hu, A. Tukker, and B. Steubing, "Future material demand for automotive lithium-based batteries." *Communications Materials*, **1**, 99 (2020).
4. A. Zeng et al., "Battery technology and recycling alone will not save the electric mobility transition from future cobalt shortages." *Nat. Commun.*, **13**, 1341 (2022).
5. A. Gutierrez, D. Tewari, J. Chen, V. Srinivasan, M. Balasubramanian, and J. R. Croy, "Review—Earth-abundant, Mn-rich cathodes for vehicle applications and beyond: overview of critical barriers." *J. Electrochem. Soc.*, **170**, 030509 (2023).
6. G. Kaur and B. D. Gates, "Review—Surface coatings for cathodes in lithium ion batteries: From crystal structures to electrochemical performance." *J. Electrochem. Soc.*, **169**, 043504 (2022).
7. A. Mukhopadhyay and B. W. Sheldon, "Deformation and stress in electrode materials for li-ion batteries." *Prog. Mater. Sci.*, **63**, 58 (2014).
8. T. Li, X. Z. Yuan, L. Zhang, D. Song, K. Shi, and C. Bock, "Degradation mechanisms and mitigation strategies of nickel-rich NMC-based lithium-ion batteries." *Electrochemical Energy Reviews*, **3**, 43 (2020).
9. T. Liu et al., "Correlation between manganese dissolution and dynamic phase stability in spinel-based lithium-ion battery." *Nat. Commun.*, **10**, 4721 (2019).
10. S. B. Son et al., "Transition metal dissolution in lithium-ion cells: a piece of the puzzle." *The Journal of Physical Chemistry C*, **127**, 1767 (2023).
11. S. Kang, S. Cho, and Y. M. Kang, "Getting to the bottom of transition metal dissolution." *Nat. Nanotechnol.*, **18**, 700 (2023).
12. J. A. Gilbert, I. A. Shkrob, and D. P. Abraham, "Transition metal dissolution, ion migration, electrocatalytic reduction and capacity loss in lithium-ion full cells." *J. Electrochem. Soc.*, **164**, A389 (2017).
13. W. Li, "Review—An unpredictable hazard in lithium-ion batteries from transition metal ions: dissolution from cathodes, deposition on anodes and elimination strategies." *J. Electrochem. Soc.*, **167**, 090514 (2020).
14. J. P. Allen, C. A. O'Keefe, and C. P. Grey, "Quantifying dissolved transition metals in battery electrolyte solutions with NMR paramagnetic relaxation enhancement." *J. Phys. Chem. C*, **127**, 9509 (2023).
15. W. B. Hawley, A. Parejiya, Y. Bai, H. M. Meyer, D. L. Wood, and J. Li, "Lithium and transition metal dissolution due to aqueous processing in lithium-ion battery cathode active materials." *Journal of Power Sources*, **466**, 228315 (2020).
16. J. C. Hestenes, J. T. Sadowski, R. May, and L. E. Marbella, "Transition metal dissolution mechanisms and impacts on electronic conductivity in composite $LiNi_{0.5}Mn_{1.5}O_4$ cathode films." *Acs Materials Au*, **3**, 88 (2023).
17. B. Zhang, L. Wang, Y. Zhang, X. Wang, Y. Qiao, and S. G. Sun, "Reliable impedance analysis of Li-ion battery half-cell by standardization on electrochemical impedance spectroscopy (EIS)." *The Journal of Chemical Physics*, **158**, 054202 (2023).
18. A. Banerjee, Y. Shilina, B. Ziv, J. M. Ziegelbauer, S. Luski, D. Aurbach, and I. C. Halalay, "On the oxidation state of manganese ions in Li-Ion battery electrolyte solutions." *J. Am. Chem. Soc.*, **139**, 1738 (2017).
19. C. Wang, L. Xing, J. Vatamanu, Z. Chen, G. Lan, W. Li, and K. Xu, "Overlooked electrolyte destabilization by manganese (ii) in lithium-ion batteries." *Nat. Commun.*, **10**, 3423 (2019).
20. H. Shin, Y. K. Lee, and W. Lu, "Structural degradation of graphite anode induced by dissolved manganese ions in lithium-ion batteries." *Journal of Power Sources*, **528**, 231223 (2022).
21. C. Zhan, T. Wu, J. Lu, and K. Amine, "Dissolution, migration, and deposition of transition metal ions in Li-Ion batteries exemplified by Mn-based cathodes—a critical review." *Energy Environ. Sci.*, **11**, 243 (2018).
22. M. Shobana, "Metal oxide coated cathode materials for li ion batteries—a review." *J. Alloys Compd.*, **802**, 477 (2019).
23. M. Chaudhary, S. Tyagi, R. K. Gupta, B. P. Singh, and R. Singhal, "Surface modification of cathode materials for energy storage devices: a review." *Surf. Coat. Technol.*, **412**, 127009 (2021).
24. C. Li, H. Zhang, L. Fu, H. Liu, Y. Wu, E. Rahm, R. Holze, and H. Wu, "Cathode materials modified by surface coating for lithium ion batteries." *Electrochimica Acta*, **51**, 3872 (2006).
25. T. F. Yi, Y. R. Zhu, X. D. Zhu, J. Shu, C. B. Yue, and A. N. Zhou, "A review of recent developments in the surface modification of $LiMn_2O_4$ as cathode material of power lithium-ion battery." *Ionics*, **15**, 779 (2009).
26. J. Lu et al., "Effectively suppressing dissolution of manganese from spinel lithium manganate via a nanoscale surface-doping approach." *Nat. Commun.*, **5**, 5693 (2014).
27. Y. Tesfamhret, R. Younesi, and E. J. Berg, "Influence of Al_2O_3 coatings on hf induced transition metal dissolution from lithium-ion cathodes." *J. Electrochem. Soc.*, **169**, 010530 (2022).
28. Z. Liu, Z. Wang, T. Lu, P. Dai, P. Gao, and Y. Zhu, "Modification of $LiNi_{0.8}Co_{0.15}Al_{0.05}O_2$ using nanoscale carbon coating." *J. Alloys Compd.*, **763**, 701 (2018).
29. H. Sun, Y. Ren, Z. Liu, Z. Chen, and S. Jia, "Enhanced electrochemical properties of $Li_{1.2}Ni_{0.13}Co_{0.13}Mn_{0.54}O_2$ coated with Al_2O_3 nano-film." *Vacuum*, **183**, 109757 (2021).
30. W. C. West, J. Soler, M. C. Smart, B. V. Ratnakumar, S. Firdosy, V. Ravi, M. S. Anderson, J. Hrbacek, E. S. Lee, and A. Manthiram, "Electrochemical behavior of layered solid solution Li_2MnO_3-$LiMO_2$ (M=Ni, Mn, Co) Li-Ion cathodes with and without alumina coatings." *J. Electrochem. Soc.*, **158**, A883 (2011).
31. H. Liu, C. Chen, C. Du, X. He, G. Yin, B. Song, P. Zuo, X. Cheng, Y. Ma, and Y. Gao, "Lithium-rich $Li_{1.2}Ni_{0.13}Co_{0.13}Mn_{0.54}O_2$ oxide coated by Li_3PO_4 and carbon nanocomposite layers as high performance cathode materials for lithium ion batteries." *J. Mater. Chem. A*, **3**, 2634 (2015).
32. A. B. Yaroslavtsev and I. A. Stenina, "Carbon coating of electrode materials for lithium-ion batteries." *Surface Innovations*, **9**, 92 (2021).
33. Z. Chen, Q. Zhang, and Q. Liang, "Carbon-coatings improve performance of li-ion battery, coating." *Nanomaterials*, **12**, 1936 (2022).
34. A. R. Han, T. W. Kim, D. H. Park, S. J. Hwang, and J. H. Choy, "Soft chemical dehydration route to carbon coating of metal oxides: its application for spinel lithium manganate." *The Journal of Physical Chemistry C*, **111**, 11347 (2007).
35. L. Jaber-Ansari et al., "Suppressing manganese dissolution from lithium manganese oxide spinel cathodes with single-layer graphene." *Adv. Energy Mater.*, **5**, 1500646 (2015).
36. H. Fei, Z. Peng, Y. Yang, L. Li, A. R. O. Raji, E. L. G. Samuel, and J. M. Tour, "$LiFePO_4$ nanoparticles encapsulated in graphene nanoshells for high-performance lithium-ion battery cathodes." *Chem. Commun.*, **50**, 7117 (2014).
37. T. Yang, N. Zhang, Y. Lang, and K. Sun, "Enhanced rate performance of carbon-coated $LiNi_{0.5}Mn_{1.5}O_4$ cathode material for lithium ion batteries." *Electrochimica Acta*, **56**, 4058 (2011).
38. E. R. Østli, Y. Tesfamhret, S. Wenner, M. J. Lacey, D. Brandell, A. M. Svensson, S. M. Selbach, and N. P. Wagner, "Limitations of ultrathin Al_2O_3 coatings on lnmo cathodes." *ACS Omega*, **6**, 30644 (2021).
39. A. Kwade, W. Haselrieder, R. Leithoff, A. Modlinger, F. Dietrich, and K. Droeder, "Current status and challenges for automotive battery production technologies." *Nat. Energy*, **3**, 290 (2018).
40. J. Hwang, K. Do, and H. Ahn, "Highly conductive 3d structural carbon network-encapsulated ni-rich $LiNi_{0.8}Co_{0.1}Mn_{0.1}O_2$ as depolarized and passivated cathode for lithium-ion batteries." *Chemical Engineering Journal*, **406**, 126813 (2021).
41. R. Pfeffer, R. N. Dave, D. Wei, and M. Ramlakhan, "Synthesis of engineered particulates with tailored properties using dry particle coating." *Powder Technology*, **117**, 40 (2001), Granulation and Coating of Fine Powders.
42. R. Sharma and G. Setia, "Mechanical dry particle coating on cohesive pharmaceutical powders for improving flowability—a review." *Powder Technology*, **356**, 458 (2019).
43. M. Naito, A. Kondo, and T. Yokoyama, "Applications of comminution techniques for the surface modification of powder materials." *ISIJ International*, **33**, 915 (1993).
44. J. A. Hersey, "Ordered mixing: a new concept in powder mixing practice." *Powder Technology*, **11**, 41 (1975).
45. S. Nadimi and M. Ghadiri, "Stress and input energy analyses of shearing a particle bed under a centrifugal field." *Powder Technology*, **394**, 575 (2021).
46. M. G. Kim and J. Cho, "Reversible and high-capacity nanostructured electrode materials for Li-Ion batteries." *Adv. Funct. Mater.*, **19**, 1497 (2009).
47. Y. Cho and J. Cho, "Significant improvement of $LiNi_{0.8}Co_{0.15}Al_{0.05}O_2$ cathodes at 60° C by SiO_2 dry coating for Li-Ion batteries." *J. Electrochem. Soc.*, **157**, A625 (2010).
48. P. Zhou, Z. Zhang, H. Meng, Y. Lu, J. Cao, F. Cheng, Z. Tao, and J. Chen, "SiO_2-coated $LiNi_{0.915}Co_{0.075}Al_{0.01}O_2$ cathode material for rechargeable li-ion batteries." *Nanoscale*, **8**, 19263 (2016).
49. C. Geng, S. Trussler, M. B. Johnson, N. Zaker, B. Scott, G. Botton, and J. R. Dahn, "A low-cost instrument for dry particle fusion coating of advanced electrode material particles at the laboratory scale." *J. Electrochem. Soc.*, **167**, 110509 (2020).
50. M. J. Herzog, N. Gauquelin, D. Esken, J. Verbeeck, and J. Janek, "Facile dry coating method of high-nickel cathode material by nanostructured fumed alumina (Al_2O_3) improving the performance of lithium-ion batteries." *Energy Technology*, **9**, 2100028 (2021).
51. J. Mun, J. H. Park, W. Choi, A. Benayad, J. H. Park, J. M. Lee, S. G. Doo, and S. M. Oh, "New dry carbon nanotube coating of over-lithiated layered oxide cathode for lithium ion batteries." *J. Mater. Chem. A*, **2**, 19670 (2014).
52. H. Bockholt, W. Haselrieder, and A. Kwade, "Intensive powder mixing for dry dispersing of carbon black and its relevance for lithium-ion battery cathodes." *Powder Technology*, **297**, 266 (2016).
53. I. H. Son, J. H. Park, S. Park, K. Park, S. Han, J. Shin, S. G. Doo, Y. Hwang, H. Chang, and J. W. Choi, "Graphene balls for lithium rechargeable batteries with fast charging and high volumetric energy densities." *Nat. Commun.*, **8**, 1561 (2017).
54. D. A. Boyd et al., "Single-step deposition of high-mobility graphene at reduced temperatures." *Nat. Commun.*, **6**, 6620 (2015).
55. H. Shin and D. Goodwin, "Deposition of diamond coatings on particles in a microwave plasma-enhanced fluidized bed reactor." *Mater. Lett.*, **19**, 119 (1994).
56. F. L. Tabares and I. Junkar, *Cold Plasma Systems and Their Application in Surface Treatments for Medicine* (Molecules, Basel, Switzerland) (2021).
57. D. G. Goodwin and J. E. Butler, "Theory of diamond chemical vapor deposition." *Handbook of Industrial Diamonds and Diamond Films*, 527 (1998).
58. T. Hong, R. Zhan, Y. Zhang, and S. Deng, "High crystallinity vertical few-layer graphene grown using template method assisted ICPCVD approach." *Nanomaterials*, **12**, 3746 (2022).
59. M. Saeed, Y. Alshammari, S. A. Majeed, and E. Al-Nasrallah, "Chemical vapour deposition of graphene—synthesis, characterisation, and applications: a review." *Molecules*, **25**, 3856 (2020).

60. S. Ghosh, S. R. Polaki, N. Kumar, S. Amirthapandian, M. Kamruddin, and K. K. Ostrikov, "Process-specific mechanisms of vertically oriented graphene growth in plasmas." *Beilstein Journal of Nanotechnology*, **8**, 1658 (2017).
61. J. Zhao, M. Shaygan, J. Eckert, M. Meyyappan, and M. H. Rümmeli, "A growth mechanism for free-standing vertical graphene." *Nano Lett.*, **14**, 3064 (2014).
62. L. B. Freund and S. Suresh, *Thin Film Materials: Stress, Defect Formation and Surface Evolution* (Cambridge University Press, Cambridge) (2004).
63. D. Peckus, R. Gudaitis, E. Rajackaitė, M. Monshi, M. Šarūnas, and S. Tamulevičius, "The quality studies of vertical graphene nanosheets catalyst-free microwave plasma-enhanced chemical vapor deposited on glass and fused silica." *Physica B: Condensed Matter*, **662**, 414957 (2023).
64. A. Cortijo and M. A. Vozmediano, "Effects of topological defects and local curvature on the electronic properties of planar graphene." *Nuclear Physics B*, **763**, 293 (2007).
65. L. G. Cançado, K. Takai, T. Enoki, M. Endo, Y. A. Kim, H. Mizusaki, A. Jorio, L. N. Coelho, R. Magalhães-Paniago, and M. A. Pimenta, "General equation for the determination of the crystallite size La of nanographite by Raman spectroscopy." *Appl. Phys. Lett.*, **88**, 163106 (2006).
66. T. R. Gengenbach, G. H. Major, M. R. Linford, and C. D. Easton, "Practical guides for x-ray photoelectron spectroscopy (XPS): Interpreting the carbon 1s spectrum." *J. Vac. Sci. Technol. A*, **39**, 013204 (2021).
67. N. Fairley et al., "Systematic and collaborative approach to problem solving using x-ray photoelectron spectroscopy." *Applied Surface Science Advances*, **5**, 100112 (2021).
68. J. C. Lascovich and S. Scaglione, "Comparison among XAES, PELS and XPS techniques for evaluation of Sp^2 percentage in a-C:H." *Appl. Surf. Sci.*, **78**, 17 (1994).
69. F. G. Bell and L. Ley, "Photoemission study of SiO_x ($0 \leqslant x \leqslant 2$) alloys." *Phys. Rev. B*, **37**, 8383 (1988).
70. D. Q. Yang, J. N. Gillet, M. Meunier, and E. Sacher, "Room temperature oxidation kinetics of Si nanoparticles in air, determined by X-ray photoelectron spectroscopy." *J. Appl. Phys.*, **97**, 024303 (2005).
71. D. Son, S. Cho, J. Nam, H. Lee, and M. Kim, "X-ray-based spectroscopic techniques for characterization of polymer nanocomposite materials at a molecular level." *Polymers*, **12**, 1053 (2020).
72. A. Kovtun, D. Jones, S. Dell'Elce, E. Treossi, A. Liscio, and V. Palermo, "Accurate chemical analysis of oxygenated graphene-based materials using x-ray photoelectron spectroscopy." *Carbon*, **143**, 268 (2019).
73. C. Woosung, S. Heon-Cheol, K. J. Man, C. Jae-Young, and Y. Won-Sub, "Modeling and applications of electrochemical impedance spectroscopy (EIS) for lithium-ion batteries." *J. Electrochem. Sci. Technol*, **11**, 1 (2020).
74. K. R. Prakasha, M. Sathish, P. Bera, and A. S. Prakash, "Mitigating the surface degradation and voltage decay of $Li_{1.2}Ni_{0.13}Mn_{0.54}Co_{0.13}O_2$ cathode material through surface modification using Li_2ZrO_3." *ACS Omega*, **2**, 2308 (2017).
75. S. Ghosh, M. Mahapatra, S. Bhowmik, K. K. Garlapati, and S. K. Martha, "Soft carbon integration for prolonging the cycle life of $LiNi_{0.5}Mn_{1.5}O_4$ cathode." *Acs Appl. Energy Mater.*, **6**, 9390 (2023).
76. F. Lin, I. M. Markus, D. Nordlund, T. C. Weng, M. D. Asta, H. L. Xin, and M. M. Doeff, "Surface reconstruction and chemical evolution of stoichiometric layered cathode materials for lithium-ion batteries." *Nat. Commun.*, **5**, 3529 (2014).
77. H. Wang, L. F. Cui, Y. Yang, H. Sanchez Casalongue, J. T. Robinson, Y. Liang, Y. Cui, and H. Dai, "Mn_3O_4 graphene hybrid as a high-capacity anode material for lithium ion batteries." *J. Am. Chem. Soc.*, **132**, 13978 (2010).
78. L. Sun, H. Song, Y. Chang, W. Hou, Y. Zhang, H. Li, and G. Han, "Effective removal of manganese in graphene oxide via competitive ligands and the properties of reduced graphene oxide hydrogels and films." *Diam. Relat. Mater.*, **114**, 108314 (2021).
79. N. A. Nebogatikova, I. V. Antonova, V. Y. Prinz, V. A. Volodin, D. A. Zatsepin, E. Z. Kurmaev, I. S. Zhidkov, and S. O. Cholakh, "Functionalization of graphene and few-layer graphene films in an hydrofluoric acid aqueous solution." *Nanotechnologies in Russia*, **9**, 51 (2014).
80. X. Yang, X. Jia, and X. Ji, "Acid induced fluorinated graphene oxide." *Rsc Adv.*, **5**, 9337 (2015).